Monthly Notices
of the
ROYAL ASTRONOMICAL SOCIETY

MNRAS **504,** 898–909 (2021)
Advance Access publication 2021 April 8

doi:10.1093/mnras/stab966

Non-Kolmogorov turbulence in multiphase intracluster medium driven by cold gas precipitation and AGN jets

C. Wang ,[1★] M. Ruszkowski,[1] C. Pfrommer ,[2] S. Peng Oh[3] and H.-Y. K. Yang[4]

[1]*Department of Astronomy, University of Michigan, 1085 S. University Avenue, 311 West Hall, Ann Arbor, MI 48109, USA*
[2]*Leibniz-Institut für Astrophysik Potsdam (AIP) An der Sternwarte 16, D-14482 Potsdam, Germany*
[3]*Department of Physics, University of California, Santa Barbara, CA 93106, USA*
[4]*Institute of Astronomy and Department of Physics, National Tsing Hua University, No. 101, Section 2, Kuang-Fu Road, Hsinchu 30013, Taiwan*

Accepted 2021 March 31. Received 2021 March 30; in original form 2020 December 22

ABSTRACT

Active galactic nuclei (AGNs) feedback is responsible for maintaining plasma in global thermal balance in extended haloes of elliptical galaxies and galaxy clusters. Local thermal instability in the hot gas leads to the formation of precipitating cold gas clouds that feed the central supermassive black holes, thus heating the hot gas and maintaining global thermal equilibrium. We perform 3D magnetohydrodynamical (MHD) simulations of self-regulated AGNs feedback in a Perseus-like galaxy cluster with the aim of understanding the impact of the feedback physics on the turbulence properties of the hot and cold phases of the intracluster medium (ICM). We find that, in general, the cold phase velocity structure function (VSF) is steeper than the prediction from Kolmogorov's theory. We attribute the physical origin of the steeper slope of the cold phase VSF to the driving of turbulent motions primarily by the gravitational acceleration acting on the ballistic clouds. We demonstrate that, in the pure hydrodynamical case, the precipitating cold filaments may be the dominant agent driving turbulence in the hot ICM. The arguments in favour of this hypothesis are that: (i) the cold phase mass dominates over hot gas mass in the inner cool core; (ii) hot and cold gas velocities are spatially correlated; (iii) both the cold and hot phase velocity distributions are radially biased. We show that, in the MHD case, the turbulence in the ambient hot medium (excluding the jet cone regions) can also be driven by the AGN jets. The driving is then facilitated by enhanced coupling due to magnetic fields of the ambient gas and the AGN jets. In the MHD case, turbulence may thus be driven by a combination of AGN jet stirring and filament motions. We conclude that future observations, including those from high spatial and spectral resolution X-ray missions, may help to constrain self-regulated AGN feedback by quantifying the multitemperature VSF in the ICM.

Key words: MHD – turbulence – galaxies: clusters: intracluster medium – galaxies: jets; galaxies: active.

1 INTRODUCTION

Hot and dilute plasmas in elliptical galaxies and galaxy clusters often exhibit cooling times shorter than the Hubble time. These short cooling times lead to local thermal instability in the hot atmospheres of these objects. The observational evidence for this instability comes in the form of detection of molecular and H α + [N II] emission from dense and cold gas (e.g. Lakhchaura et al. 2018; Pulido et al. 2018; Babyk et al. 2019; Olivares et al. 2019). The systems containing the cold gas are characterized by relatively shorter radiative cooling times, higher overall gas density, lower entropies, and less symmetric X-ray emissivity distributions caused by gas motions (e.g. Lakhchaura et al. 2018). While there continues to be a debate on whether in the locally thermally unstable systems, the ratios of the cooling time to the free-fall time are systematically lower [see Lakhchaura et al. (2018) for evidence in favour of this hypothesis and Babyk et al. (2019) for the opposing view], there is emerging consensus that the cold gas has cooled out of the hot plasma.

Since the cool and thermally unstable gas is expected to be unsupported by the pressure gradients in the hot gas phase, the cold phase precipitates and feeds the central supermassive black holes (e.g. Werner et al. 2013, 2014). There is well-established evidence for active galactic nuclei (AGNs) feedback from black holes in the systems characterized by short radiative cooling times. For example, recent LOFAR observations by Bîrzan et al. (2020) of X-ray cavity systems present in such systems confirm that there is a connection between radio emission and AGN jet power inflating the cavities.

Observations of cold gas precipitation and AGN feedback in these systems have spurred theoretical investigations aiming to explain the feedback cycle. Using idealized numerical experiments in which heating was distributed globally to balance cooling in the time average sense, McCourt et al. (2012), Sharma et al. (2012), and Gaspari, Ruszkowski & Oh (2013) demonstrated that heated atmospheres can remain in global thermal equilibrium while exhibiting local thermal instability. In these models, thermal instability led to precipitation of cold gas, feeding of the central engine, and subsequent heating to balance radiative cooling globally. Using analytic methods to interpret recent simulations of feedback, Voit et al. (2017) considered two condensation modes – (i) precipitation and infall and (ii) uplift of ambient gas by outflows followed by

---

★ E-mail: wangcha@umich.edu

Published by Oxford University Press on behalf of Royal Astronomical Society

condensation – and argued in favour of the former. An alternative suggestion was made by McNamara et al. (2016) who proposed that cold clouds condense out of the low-entropy gas uplifted by the AGN bubbles.

Hydrodynamical AGN feedback simulations including bipolar jet outflows were performed by Gaspari, Ruszkowski & Sharma (2012), Prasad, Sharma & Babul (2015), Li, Ruszkowski & Bryan (2017), Martizzi et al. (2019), and Wang, Li & Ruszkowski (2019). These simulations were successful in establishing (i) self-regulating feedback cycle, where the balance of cooling and heating was achieved globally, and where the amount of energy injected by the jets was regulated by the amount of accretion of the cold gas, and (ii) predicting density, temperature, and entropy profiles in agreement with the observations. In particular, the simulations by Wang et al. (2019) of self-regulated AGN feedback can maintain the observed properties of single and multiphase haloes, which is consistent with analytical models (Voit et al. 2015) and recent observations (Frisbie et al. 2020). Using a similar approach, albeit excluding the formation of the cold phase clouds, Yang & Reynolds (2016a) performed a careful analysis of various contributions to the AGN heating budget. Specifically, they demonstrated that a substantial contribution to heating comes from shock heating and turbulent mixing (inside the jet cones) and weak shocks and adiabatic compression (outside the jet cones). The importance of sound wave heating was recently put on a firmer footing (Bambic & Reynolds 2019, see also Ruszkowski, Brüggen & Begelman 2004b,a).

The nature of the simulated AGN feedback cycle and the properties of the multiphase gas depend on the physics included in the simulations. Recent results by Beckmann et al. (2019) demonstrate that while both the precipitation and uplift of dense gas is present in the simulated atmospheres, purely hydrodynamical simulations struggle to regulate the cluster cooling-feedback cycle and lead to very clumpy distributions on cold gas that is inconsistent with the very filamentary cold structures seen in the observational data. These findings underscore the importance of investigating the impact of a wider array of physical processes in the simulations. Qiu et al. (2019) performed hydrodynamical simulations of self-regulated feedback including the effects of radiation feedback, and while they observed the formation of elongated filaments, the simulations also resulted in the formation of overly massive cold central discs.

Magnetohydrodynamical (MHD) simulations of AGN jet feedback with super-Lagrangian resolution and including the effect of cosmic ray (CR) pressure were performed by Weinberger et al. (2017). Single injection AGN events were studied using CR MHD simulations including CR diffusion and Alfvén wave cooling, thus emulating CR streaming, by Ehlert et al. (2018), who concluded that CR heating rates were significant compared to cooling and matched radial CR pressure profiles of 1D steady-state CR heating models (Jacob & Pfrommer 2017a,b, see also Guo & Oh 2008). The CR pressure of AGN lobes is also consistent with the missing thermal pressure as inferred from Sunyaev-Zel'dovich observations of the extreme AGN outburst in MS0735 (Abdulla et al. 2019; Ehlert et al. 2019; Yang, Gaspari & Marlow 2019). CR MHD simulations of self-regulated AGN jet feedback cycle including the effects of CR streaming, and associated with it CR heating of the gas, were performed by Ruszkowski, Yang & Reynolds (2017) and Wang, Ruszkowski & Yang (2020), who demonstrated that CR could serve as a dominant heating agent to keep the atmospheres in global thermodynamical equilibrium. Wang et al. (2020) also demonstrated that the magnetic fields play a crucial role in angular momentum redistribution via magnetic breaking of the precipitating cold gas, which allows the gas to accrete and feed the central supermassive black hole without invariably forming massive cold central tori. More broadly, this suggest that the magnetic fields may play a role in shaping the statistical properties of the velocity distribution of the gas in these systems.

As mentioned above, AGN feedback, cold gas precipitation, and the physics relevant to the problem of the feedback cycle are all intricately related to the question of turbulence in the atmospheres of galaxies and clusters. Thus turbulence measurements could provide constraints on how the AGN feedback works in realistic systems. A recent review of turbulence in the hot haloes of ellipticals and clusters has been presented by Simionescu et al. (2019). Constraints on the level of turbulence have been obtained from non-spatially resolved line broadening. Sanders & Fabian (2013) reported velocity limits of 300–500 km s^{-1} in elliptical galaxy atmospheres. Using a combination of resonant scattering and line broadening, Ogorzalek et al. (2017) measured turbulent velocities in the hot haloes of giant ellipticals and found typical Mach numbers of $\sim$0.45. Direct measurements of the level of turbulence in the Perseus cluster obtained using the Hitomi mission (Hitomi Collaboration 2016, 2018) are consistent with relatively low level of turbulence in this cluster. Future high spectral and spatial resolution X-ray missions may be able to quantify the level of turbulence in significantly more detail by measuring the velocity power spectrum or velocity structure function (VSF) of the hot gas phase (Zhuravleva et al. 2012; ZuHone, Markevitch & Zhuravleva 2016). Recently, a very promising alternative approach to constraining turbulence has been presented by Li et al. (2020), who measured the VSF of the cold gas phase and showed that the slope of the cold phase VSF departs from the Kolmogorov prediction. Motivated by these observations, Hillel & Soker (2020) simulated the VSF in non-radiative simulation of AGN jet outburst and concluded that the VSF is steeper than that expected based on the Kolmogorov theory of turbulent cascade. In this paper, we study via MHD simulations of the self-regulated AGN feedback, the properties of turbulence in the hot and cold phases of the intracluster medium (ICM). In particular, we discuss the coupling between the two gaseous phases and the mechanisms driving turbulence in these phases, and make predictions for the slope of the cold phase VSF, and its relationship to the hot phase counterpart. The paper is organized as follows. In Section 2, we present the simulation approach. The discussion of the results is presented in Section 3, and we conclude in Section 4.

2 METHODS

We perform 3D MHD simulations using the FLASH code (Fryxell et al. 2000; Dubey, Reid & Fisher 2008) using the directional unsplit staggered mesh MHD solver (Lee & Deane 2009; Lee 2013). We adopt a simulation domain with statically refined grids. Similar to Wang et al. (2020), the domain is refined by a set of nested cubic regions. The entire domain is a cubic region with width $L_{\mathrm{box}} = 1$ Mpc and 64^3 base grids. The central regions with width

$$L_n = L_{\mathrm{box}}/2^n \text{ kpc} \tag{1}$$

have n additional nested refinement levels. We include models with different $n_{\max}$, as listed in Table 1. The size of the smallest cell is $\Delta x_{\min} = L_{\mathrm{box}}/64/2^{n_{\max}}$. For the resolution study, we modify the width of the two most refined regions in the high resolution models, so that L_7 in the high resolution models equals $L_6 \approx 15.6$ kpc in the low resolution models. Therefore, in order to calculate the sizes of the regions at a given refinement level in the fiducial hydrodynamical (FID-HD) and fiducial (FID-MHD cases, we use equation (1) for n

Table 1. List of models.

Name	Magnetic field	n_{max}	Δx_{min}
LR-HD	No	6	0.244 kpc
LR-MHD	Yes	6	0.244 kpc
FID-HD	No	7	0.122 kpc
FID-MHD	Yes	7	0.122 kpc

≤ 5 and set $L_7 \approx 15.6$ kpc and choose L_6 such that it falls between L_5 and L_7 (our adopted value of L_6 is $\approx$23.4 kpc).

We use the diode boundary conditions, where all variables have zero gradient and gas can only flow out at the domain boundary.

2.1 Cluster initial conditions

We setup the initial conditions of the hot gaseous halo consistent with the Perseus cluster. For the temperature profile, we use an analytical fit based on the observed X-ray surface brightness distribution in the Perseus cluster (Churazov et al. 2003):

$$T(r) = 7\ \mathrm{keV}\frac{1 + (r_{\mathrm{kpc}}/71)^3}{2.3 + (r_{\mathrm{kpc}}/71)^3}[1 + (r_{\mathrm{kpc}}/380)^2]^{-0.23}. \quad (2)$$

We include a static gravitational field with contributions from a dark matter halo and stars. The dark matter potential is described by an NFW profile (Navarro, Frenk & White 1996), with scale radius $r_{\mathrm{s}} = 358.3$ kpc, virial radius $r_{\mathrm{vir}} = 2.44$ Mpc, and virial mass $M_{\mathrm{vir}} = 8.5 \times 10^{14}\,\mathrm{M}_{\odot}$. The gravitational acceleration due to stars is based on the analytical fit to the de Vaucouleurs profile (Mathews, Faltenbacher & Brighenti 2006):

$$g_{\mathrm{star}}(r) = \left[\frac{r_{\mathrm{kpc}}^{0.5378}}{2.853 \times 10^{-7}} + \frac{r_{\mathrm{kpc}}^{1.738}}{1.749 \times 10^{-6}}\right]^{-1.11} \mathrm{cm\ s}^{-2}. \quad (3)$$

Assuming hydrostatic equilibrium, we then calculate the density profile and normalize it to match the azimuthally averaged observed density profile (Mathews et al. 2006).

Following Ruszkowski et al. (2007), we set up tangled magnetic fields with power spectrum $B_k \propto k^{-11/6}\exp(-k^4/k_0^4)$, where $k_0 = 100(2\pi/L_{\mathrm{box}})$. To obtain magnetic fields with this power spectrum and plasma $\beta \sim 100$, we first inversely Fourier transform the power spectrum to real space; then normalize the real space magnetic fields to have $\beta \sim 100$; Fourier transform the magnetic fields; clean the magnetic field divergence in Fourier space; and finally perform inverse Fourier transformation to obtain real space magnetic fields. We repeat this procedure until the magnetic fields become divergence free. For radiative cooling, we adopt the tabulated Sutherland-Dopita cooling function assuming one-third solar metallicity (Sutherland & Dopita 1993).

2.2 AGN feedback

We use the cold accretion model to simulate the fuelling of the AGNs. The cold gas is accreted at a rate of $\dot{M}_{\mathrm{acc}} = M_{\mathrm{acc}}/5$ Myr, where M_{acc} is the total mass of the cold gas ($T < 10^5$ K) within the depletion region, $r < 1.2$ kpc. For each computational time step (Δt), $\dot{M}_{\mathrm{acc}}\Delta t$ of the cold gas is removed in the depletion region and loaded to the jet base. The gas in the jet base is then launched into the halo via bipolar jets along z-axis of the simulation domain. The jet base is a cylinder at the domain centre with a radius of 1.25 kpc and a height of 4 kpc. We assume a jet precession angle of 15 deg and a period of 10 Myr. The AGN feedback is purely kinetic with power $\dot{E}_k = \epsilon\eta\dot{M}_{\mathrm{acc}}c^2$, where $\epsilon = 10^{-3}$ is the feedback efficiency, $\eta = 1$ is the mass loading factor, and c is the speed of light.

3 RESULTS

3.1 General characteristics of cold gas distribution and the evolution of the cluster

In all cases, the systems go through the self-regulated AGN feedback cycles. The development of thermal instabilities leads to cold gas condensation in the form of filaments. The cold gas forms a long-lived massive rotating disc during the long-term evolution of the hydro cases, while the disc is absent in the MHD cases. The same phenomenon was found in Wang et al. (2020). As we argued there, the formation of such a disc is unphysical and in tension with observations. The magnetic tension force can effectively decelerate the cold gas. Therefore, the magnetic fields redistribute the angular momentum of the cold gas, and prevents disc formation.

Snapshots of the projected gas density are shown in Fig. 1 in the FID-HD and FID-MHD case (left-hand and right-hand panel, respectively). There are clear morphological differences between these two cases. While in the hydro case, the dense and cold gas exists in the form of blobs and filaments, in the MHD case, the dense gas structures are noticeably more filamentary. In both cases, the filaments tend to be biased in the radial direction. The cold filaments are more spatially confined to the cluster centre in the MHD cases than those in hydro cases (Fig. 1).

In the FID-MHD runs, 95 per cent of the cold gas mass is contained within $r \lesssim 25$ kpc, while for FID-HD, this happens within $r \lesssim 30$ kpc (grey lines in Fig. 2; hereafter cold gas is defined as having $T < 2 \times 10^4$ K and $\rho > 10^{-24}$ g cm^{-3}, and hot gas as having 10^7 K $< T < 10^8$ K). When the system is active, the typical mass of the cold gas is $10^{10} \sim 5 \times 10^{10}\,\mathrm{M}_{\odot}$, which is broadly consistent with the high end of the molecular gas mass observed in galaxy clusters (e.g. Vantyghem et al. 2018; Olivares et al. 2019). This is especially so given that our definition of the cold gas includes the molecular gas as well as the gas at higher temperatures. We also note that, as evidenced in Fig. 2, the time averaged amount of cold gas is smaller in the FID-MHD cases compared to the FID-HD case.

For all four runs, the typical 1D velocity dispersion of the hot gas during the AGN active phase in the 30 kpc $< r <$ 60 kpc region is $\sim$100 km s^{-1}, which is consistent with other hydrodynamic simulations (Prasad, Sharma & Babul 2018) but underestimates the Hitomi observation (Hitomi Collaboration 2016). In the $r <$ 10 kpc region, the dispersion is $\sim$200 km s^{-1}. Our results thus suggest that AGN-related activities may be the dominated driver of turbulence in the ICM centre, but can not account for the turbulence observed in the outer region of the ICM halo, where large-scale motions such as cosmic accretion and mergers may be the major contributor (Ruszkowski et al. 2011; Lau et al. 2017; Bourne, Sijacki & Puchwein 2019) with possibly important contributions from orbiting substructures (Bourne & Sijacki 2017) and magnetic tension forces resulting from MHD turbulence (Ehlert et al. 2021).

In the left-hand panel of Fig. 3, we show radial profiles of the magnetic pressure ('x'-labelled line) and thermal pressure (dot-labelled line) of the cold gas in the MHD runs. The right-hand panel shows the profiles of the same quantities but for the hot gas. In the $r <$ 10 kpc region, the average plasma β reduces to $\sim$10 from the initial value of $\sim$100. With $\beta \sim$ 10, there is an energy equal partition between kinetic energy and magnetic energy in the hot halo. Therefore, the magnetic fields are globally amplified by

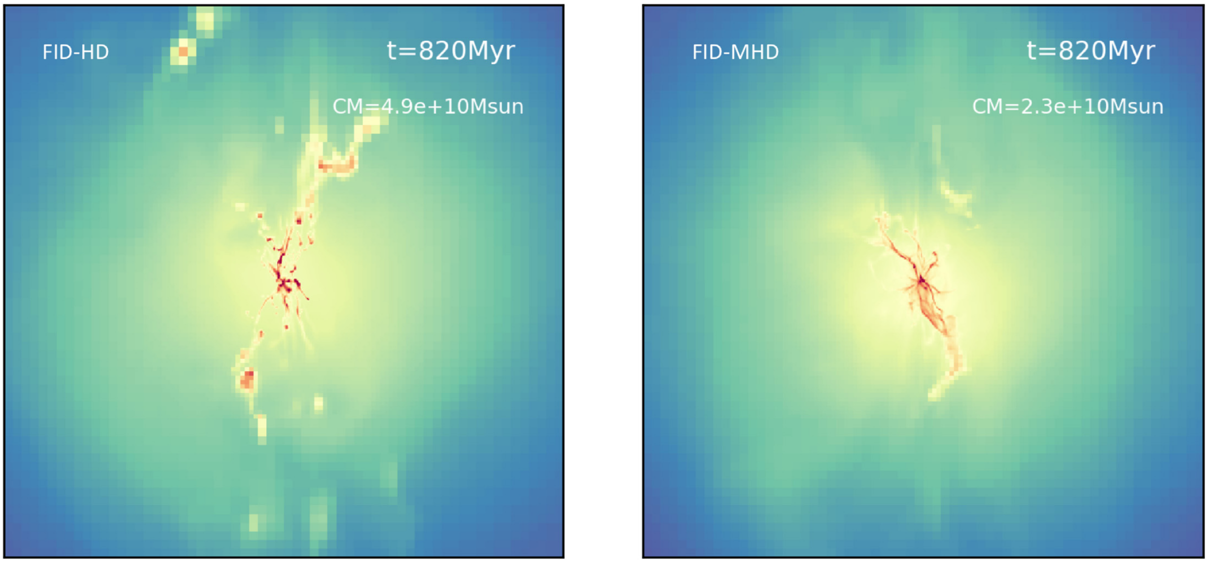

Figure 1. Snapshots of the projected gas density from our fiducial hydrodynamical (FID-HD; left) and fiducial MHD (FID-MHD; right) runs. The projection is done along the *x*-axis and within the central 125 kpc-wide cube. It is clear that cold filaments are more spatially confined in FID-MHD than FID-HD.

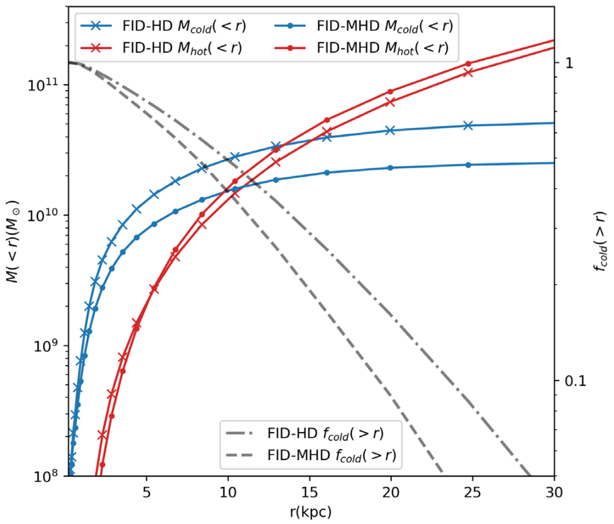

Figure 2. Blue and red lines: radial profile of enclosed mass ($M < (r)$) of hot and cold gas in FID-HD and FID-MHD cases. Grey lines: the profiles of cold gas fraction outside of a given radius ($f_{\rm cold}(> r)$). All profiles are averaged over $t = 0.4$–1.5 Gyr.

turbulent stirring in the hot halo and lose memory of the initial conditions. It is clear from this figure that the pressure support of the cold filaments is dominated by the magnetic pressure. The magnetic pressure of the cold filaments is in balance with the thermal pressure of the ambient hot gas, which is evident from comparing top orange line in the left-hand panel (representing magnetic pressure) with the top orange line in the right line (representing thermal pressure) – both of these curves have very similar values in the central ∼20 kpc. This result is in agreement with the optical emission line observations of Perseus cluster (Fabian et al. 2008) and numerical simulations (Sharma, Parrish & Quataert 2010). Furthermore, the low plasma β filaments are consistent with the models suggesting that the H α emission of the cold filaments is powered by magnetic reconnection (Churazov, Ruszkowski & Schekochihin 2013) or CRs (Ruszkowski, Yang & Reynolds 2018).

3.2 Velocity structure function

Throughout this paper, we use the first order VSF of the *x*-component to study the properties of the ICM turbulence. It is defined as $\mathrm{VSF}(l) \equiv \langle|v_x(\mathbf{r}+\mathbf{l}) - v_x(\mathbf{r})|\rangle$, where v_x, $\boldsymbol{r}$, and $\boldsymbol{l}$ are the *x*-component of the gas velocity, position vector, and the vector connecting a pair of points, respectively, and the averaging is performed over pairs of points with the same separation $l = |\boldsymbol{l}|$. We note that the *y*-component VSF shows qualitatively the same results due to the axisymmetry about the jet launching *z*-axis. We denote the slope of the VSF as m_p, i.e. $\mathrm{VSF}(l) \propto l^{m_p}$. For all the VSFs calculated in this paper, we only use the data in the region with the highest refinement level. This approximately corresponds to the central $r <$ 10 kpc region for all runs. Thus we ensure a uniform sampling of the velocity fields without interpolations. In this paper, we focus on 3D VSF and on how the physics included in the simulations affects the VSF slope. Thus, our results can be compared to the prediction from the Kolmogorov theory in a straightforward fashion.

3.2.1 *Velocity structure function of the precipitating cold gas*

Fig. 4 shows the first order VSFs averaged over the AGN active phase ($t = 0.5$–1 Gyr). The right four panels are the same as the left four except that they are normalized to 1 at the separation of 2 kpc. We include the normalized version in order to make it easier to compare the VSF slopes. One of our key results is that the averaged VSF of cold filaments ($T < 2 \times 10^4$K, $\rho > 10^{-24}$ g cm^{-3}) has a slope steeper than that predicted from the Kolmogorov turbulence, $m_{\rm kol} =$ 1/3. In the hydro cases, the slope is $m_p \approx 1/2$; and in the MHD cases, the slope is either close to 1/2 or slightly shallower. Comparisons of blue curves in the LR-HD and FID-HD cases (top row), and of the blue curves in the LR-MHD and FID-MHD cases (bottom row), demonstrate the slopes of the cold phase VSF are numerically convergent in the inertial range (2–4 kpc in low-resolution and 0.8–3 kpc in fiducial cases).

In order to understand the nature of this scaling of the velocity with cloud separation, we inspect the acceleration terms in the Euler equation for an isolated cold filament. According to the momentum equation, the average acceleration acting on the filament

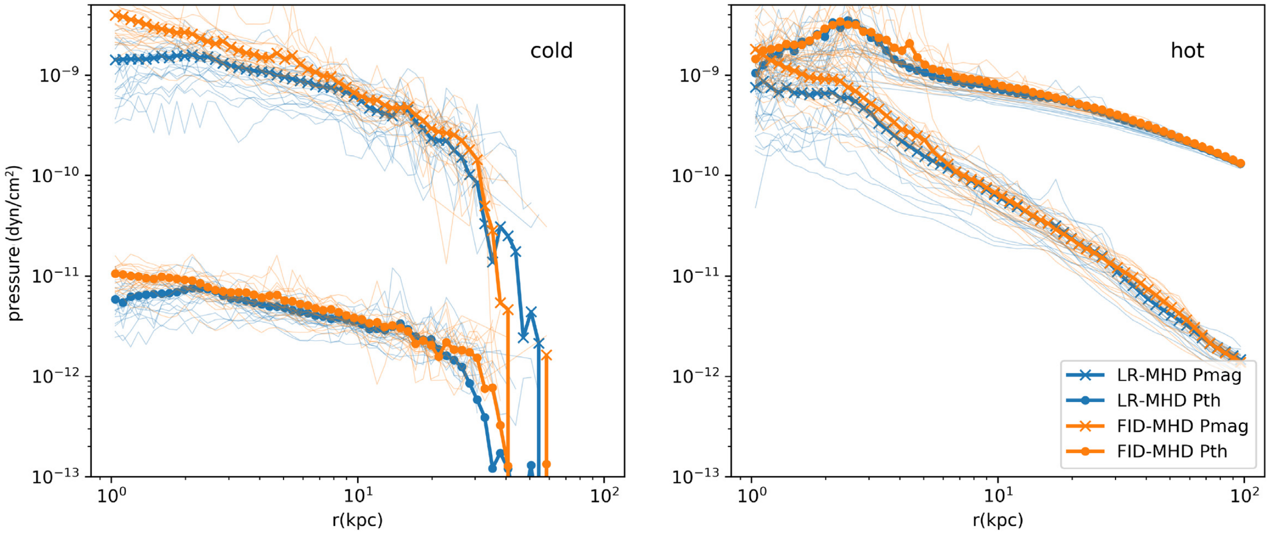

Figure 3. Left: radial profile of the magnetic pressure (‘x’-labelled line) and thermal pressure (dot-labelled line) of the cold gas in the MHD runs. Right: same as on the left but for the hot gas.

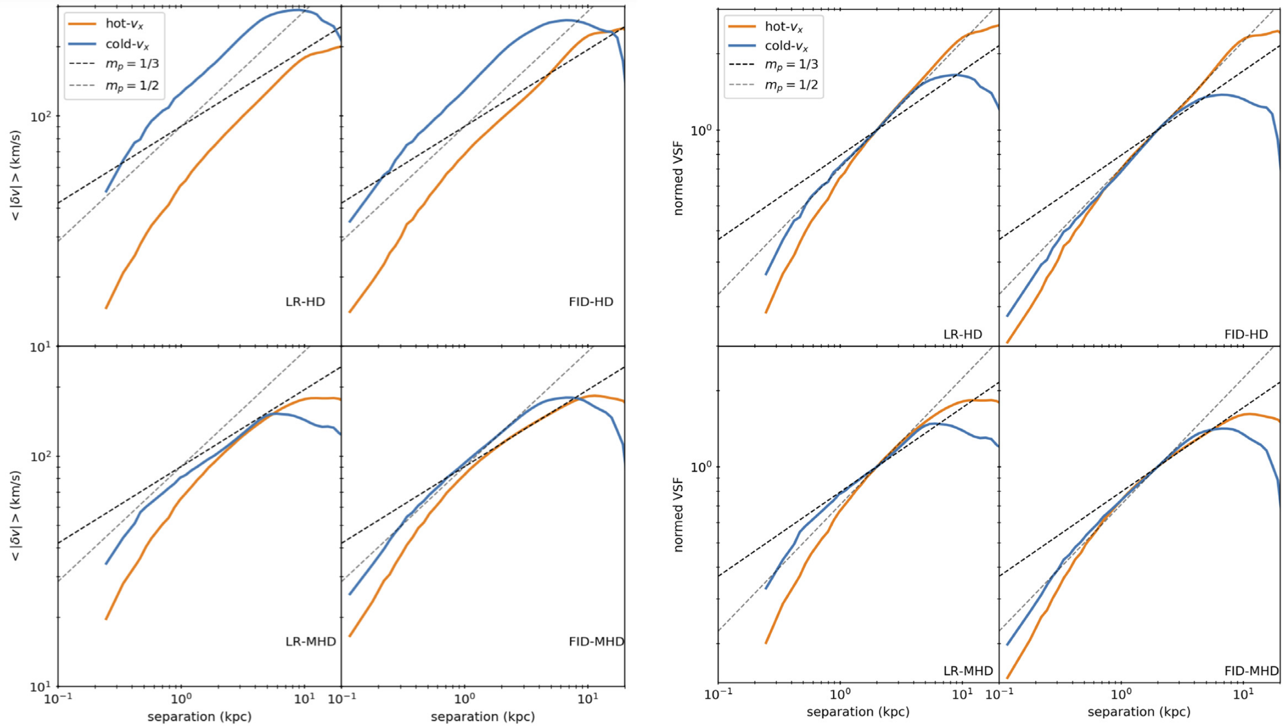

Figure 4. VSFs of hot (orange) and cold (blue) phase gas averaged over $t = 0.5$–1 Gyr of the four runs. The right four panels are the same as the left four except that they are normalized to 1 at the separation of 2 kpc. The black and grey dashed lines have slopes $m_p = m_{\mathrm{kol}} = 1/3$ and $m_p = 1/2$, respectively.

can be decomposed into: gravity (a_g), magnetic tension (a_t), thermal pressure gradient (a_p), magnetic pressure gradient (a_m), and the ram pressure (a_{rp}). The accelerations are calculated from:

$$\boldsymbol{a}_g = \frac{1}{M}\int \rho \boldsymbol{g} \mathrm{d}V \tag{4}$$

$$\boldsymbol{a}_t = \frac{1}{M}\int \rho \nabla \cdot \left(\frac{\boldsymbol{BB}}{4\pi}\right) \mathrm{d}V \tag{5}$$

$$\boldsymbol{a}_p = -\frac{1}{M}\int \nabla p_{\mathrm{th}} \mathrm{d}V \tag{6}$$

$$\boldsymbol{a}_m = -\frac{1}{M}\int \nabla p_{\mathrm{mag}} \mathrm{d}V, \tag{7}$$

$$\boldsymbol{a}_{\mathrm{rp}} = -\frac{1}{M}\rho_{\mathrm{ICM}} v_{\mathrm{com}}^2 S, \tag{8}$$

where the integral is over the filament; ρ is the gas density; $\boldsymbol{g}$ is the gravitational acceleration; $\boldsymbol{B}$ is the magnetic field strength; $M = \int \rho \mathrm{d}V$ is the total mass of the filament; p_{th} is the thermal pressure; p_{mag} is the magnetic pressure; ρ_{ICM} is the density of ambient ICM; v_{com} is the centre of mass velocity of the filament; and S is the

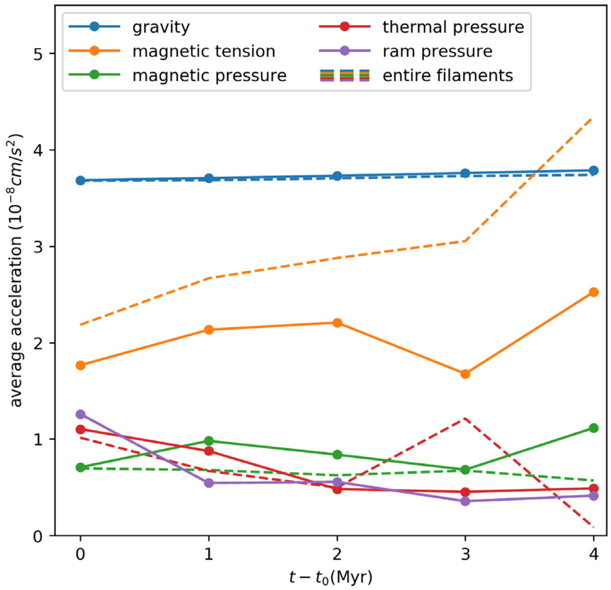

Figure 5. Values of accelerations contributed by different sources during the infall process of a cold filament. The solid lines show the values averaged over the head of the filament and the dashed lines are over the entire filament.

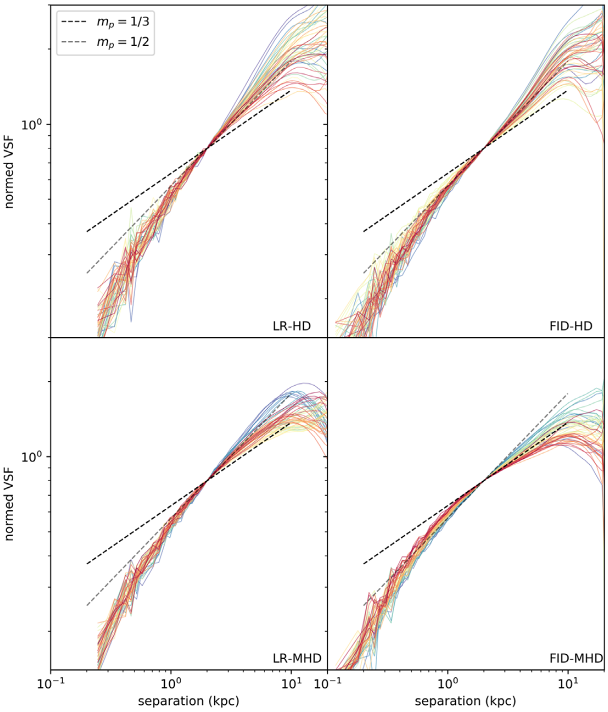

Figure 6. Hot phase VSFs plotted every 10 Myr for $t = 0.5$–1 Gyr in four runs. Time is denoted by the colour, changing from purple to red.

surface area of the cross-section normal to $v_{\rm com}$ of the filament. We estimate $\rho_{\rm ICM} = 2 \times 10^{-25}\,{\rm g\,cm^{-3}}$. As the filament falls towards the halo centre, it is elongated due to the deceleration from magnetic tension force and forms a tail behind the head of the filament. The magnitudes of all the acceleration vectors are shown in Fig. 5. The solid lines are the accelerations averaged over the the head of the filament and the dashed lines are over the entire filament (note that selecting the entire filament or just its head has little effect on $a_{\rm rp}$; filament head is defined as the location in the filament closest to the cluster centre). This analysis shows that when magnetic fields are absent, the motion of the cold filament is dominated by the gravitational force. Gravitational acceleration close to the cluster centre is nearly constant. The velocity v of the cold filaments subject to constant gravitational acceleration, g, scales with travel length L as $v \propto (gL)^{1/2}$, which leads to the $m_p \approx 1/2$ slope of the VSF in the hydro runs. We verify this hypothesis by performing a simple experiment where we calculate the VSF of multiple 1D velocity–position pairs sampled from a free-fall trajectory (see Appendix B for details). When magnetic fields are included, the sub-dominant magnetic tension force increases as the filaments fall, which effectively makes the filaments gain less velocity for the same travel length compared with the hydro case. Therefore, $m_p < 1/2$ for cold phase in the MHD cases.

3.2.2 Velocity structure function of the hot ICM

The hot phase discussed hereafter has the temperature in the range $10^7\ {\rm K} < T < 10^8\ {\rm K}$ and excludes the gas component directly entrained by the bipolar jets. We define the entrained gas as the gas which has fast outflow velocity along the jet launching axis, i.e. ${\rm sign}(z)v_z > 500$ km/s, where v_z is the gas velocity along z-axis.

In general, the turbulence in the hot ICM is volume filling. We estimate the degree of volume filling following Iapichino & Niemeyer (2008), where the volume filling factor (f_V) is defined as the fraction of the volume of the gas that has vorticity magnitude larger than the mass-weighted average vorticity. We find $f_V \sim 0.4$ for hot gas in both FID-HD and FID-MHD runs, indicating moderately volume filling turbulence.

In the hydro cases, when the system is active (i.e. when the AGN jet is switched on and cold gas precipitation is present), the slope of the hot phase VSF scatters around $m_p = 1/2$. This can be seen in Fig. 6, which shows the hot phase VSFs during the active phases (for the hydro cases, see top two panels in this figure) and the average VSF has the same slope as that of the cold phase in the inertial range (top two panels of Fig. 4). This result is numerically convergent and is consistent with the possibility that it is the cold filaments that predominantly drive turbulence in hot gas (see also Section 3.3 below). Note that the steep slope of hot phase VSF is not likely caused by the superposition of turbulence with multiple injection scales. Yoo & Cho (2014) perform turbulent simulations adopting multiple injection scales by design, and find that the kinetic energy power spectra show spiky features in the injection scales range and the spectra in the inertial range are still Kolmogorov-like. The hot VSFs in our simulations do not have these features. In the quiescent phase, the hot VSF flattens towards $m_{\rm kol}$ on large scales (Fig. 7). We note that the same steepening/flattening trends in the active/quiescent phases are also present in the MHD cases, which we do not show in this figure in the interest of brevity.

In the MHD cases, when system is in the active phase, the hot phase VSFs have slopes scattering around $m_p = 1/2$ in LR-MHD case, while in the FID-MHD case, the VSFs are systematically shallower and the slopes are scattered between $m_p \lesssim 1/3$ to $m_p \approx 1/2$ (two bottom panels in Fig. 6). Although not numerically convergent, in both MHD cases, the hot phase slopes m_p are generally distributed above 1/3 predicted from Kolmogorov theory. In Appendix A, we verify via a simple controlled experiment that the expected slope of the hot phase VSF is indeed 1/3 and we assess at what minimum separations the numerical effects become important. In this experiment, we find the Kolmogorov-like VSFs steepen at sub-kpc scales due to numerical

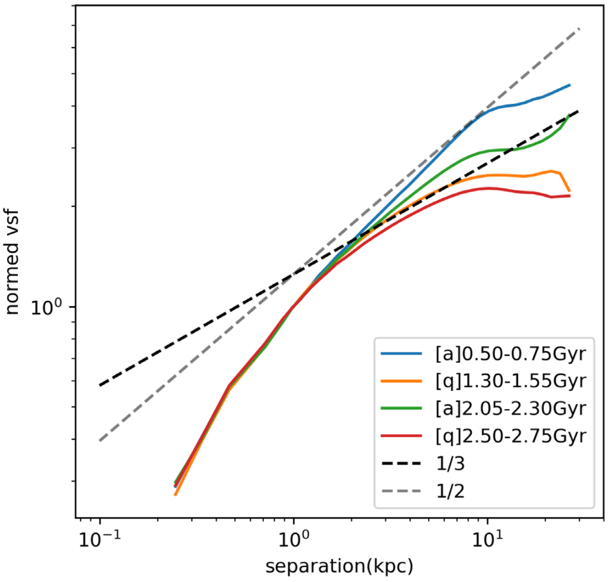

Figure 7. Normalized VSF of the hot gas averaged over quiescent and active epochs in the LR-HD case. Each VSF is labelled with active ('[a]') or quiescent ('[q]') epoch and the corresponding time range in the legend.

dissipation, which explains the same steepening in the hot VSFs of full physics runs (Fig. 4). Note that cold-phase VSFs are less affected by the numerical steepening at small scales. This is because gravity dominates the motion of cold filaments (Fig. 5); and gravity is insensitive to numerical resolution. This is consistent with the fact that the slope of cold phase VSF is numerically convergent in both hydro and MHD cases. In general, in full physics simulations, the slopes of the hot phase VSF in the MHD cases are shallower than 1/2. There appears to be tentative evidence for the flattening of the hot phase VSF in the MHD case towards the 1/3 slope expected in the Kolmogorov case. However, we note that we cannot make definite statement about the slope of the hot phase VSF due to relatively narrow inertial range and limited numerical resolution. We further discuss the driving of the hot phase turbulence in Section 3.3.

As mentioned above, here we focus on 3D VSF and the physics shaping the VSF slope. This allows us to *directly* compare simulation results to the prediction from the Kolmogorov theory. In order to make detailed comparisons to the observations of the VSF of the cold and hot phases of the ICM, one needs to perform careful projections on to the plane of the sky. As far as the hot phase VSF is concerned, ZuHone et al. (2016) demonstrate that, while the projected and 3D velocity power spectra have the same slope, the second order 3D VSF has a steeper slope than 2/3 predicted from Kolmogorov's theory. Thus, we expect that the first order projected hot phase VSF could also have a steeper slope than its Kolmogorov's counterpart. Although the hot gas power spectra from X-ray observations can be corrected for the projection effect, there are difficulties with doing direct comparison between our results and the current X-ray observations. First, the X-ray analysis of power spectra (e.g. Zhuravleva et al. 2014) do not cover the $r \lesssim 10$ kpc region of the ICM halo, where the VSFs in our simulations are calculated. Secondly, observed turbulence in the hot phase is derived from the density fluctuations by assuming an isobaric equation of state and no other sources of density fluctuations. However, tangential discontinuities (including but not limited to bubble-ICM discontinuities or cold fronts) can source density fluctuations but without contributing to velocity fluctuations, thus causing bias in the turbulence derivation. For the cold phase, the projected slope may be shallower than the slope of the 3D VSF (Li et al. 2020). The relationship between the 2D and 3D slope may be further complicated in this case by the fact that many filaments may be seen along the same line of sight. Maps of the distribution of the cold filaments on the sky used to compute the VSF by Li et al. (2020) suggest that the covering factor may exceed unity. It is for these reasons that we defer the projection analysis to future work and in this paper, we instead focus on the physics of the 3D VSF and comparisons to the prediction from the Kolmogorov theory.

3.3 The driving sources of turbulence in the hot ICM

We now consider two turbulence driving mechanisms that operate in the hot phase and discuss their relative importance depending on the physics included in the simulations. Note that there are other possible driving sources of turbulence in the ICM, such as cosmological mergers (Lau et al. 2017; Bourne et al. 2019), orbiting substructures (Bourne & Sijacki 2017), penetrating gas streams (Zinger et al. 2016), gas sloshing (ZuHone et al. 2018), and magnetic tension forces resulting from MHD turbulence driven by any of the effects above (Ehlert et al. 2021). However, these sources should be less important in the central region of the ICM considered here.

3.3.1 Turbulence driving by cold filaments

It is conceivable that cold filaments stir the ambient hot gas and generate turbulence. The arguments in favour of this hypothesis are the following:

(i) The cold phase mass has a dominant contribution to the mass budget in the inner core of ICM. Specifically, as shown by the blue and red lines in Fig. 2, the cold gas mass exceeds the hot gas mass for radii $r < 10$ kpc in the FID cases, and we see smaller amounts of cold gas in the FID-MHD case compared to the FID-HD case. Using Chandra observations, Babyk et al. (2019) show that the ratio of molecular gas to atmospheric gas within a 10 kpc radius lies between 3 per cent and 50 per cent for central galaxies in clusters. As mentioned above, our definition of the cold gas includes the molecular gas and the gas at higher temperatures, so the cold gas portion in our simulations may be broadly consistent with the observations. Thus, in the inner region, the cold filaments have sufficient momentum and may be capable of driving the motion of the hot phase.

(ii) Hot and cold gas velocities are spatially correlated. The spatial correlation is defined as: $f_{\rm ch}(r) = \langle \boldsymbol{v}_{\rm hot}(\boldsymbol{x}) \cdot \boldsymbol{v}_{\rm cold}(\boldsymbol{x}+\boldsymbol{r})\rangle_{\boldsymbol{x}}$, where $r = |\boldsymbol{r}|$. This quantity is positive and increases with decreasing spatial separation (Fig. 8), indicating that the velocities of the cold and hot gas parcels are more aligned when they are closer. Thus, the motions of cold filaments and hot gas are *coupled*.

(iii) In the hydro cases, when the system is in the active phase, the slope of hot phase VSF is $m_p \sim 1/2$, which is the same as the average VSF slope of the cold gas in the inertial range.

(iv) The distributions of the hot and cold gas velocities are radially biased. The anisotropy parameter is defined as: $\beta = 1 - \sigma_{\rm tan}^2/2\sigma_{\rm rad}^2$, where $\sigma_{\rm tan}^2 = \sigma_\theta^2 + \sigma_\phi^2$. The motion of the cold filaments is highly radial due to the radial gravity and launching of the thermally unstable blobs by the AGN jets. The motion of the hot gas is also radial ($\beta > 0$; Fig. 9). This is so despite the fact that the hot gas entrained by the AGN jets is filtered out in the process of computing β. This implies coupling between the radially-biased cold filaments and hot phase. This conclusion is further strengthened by noting that in the

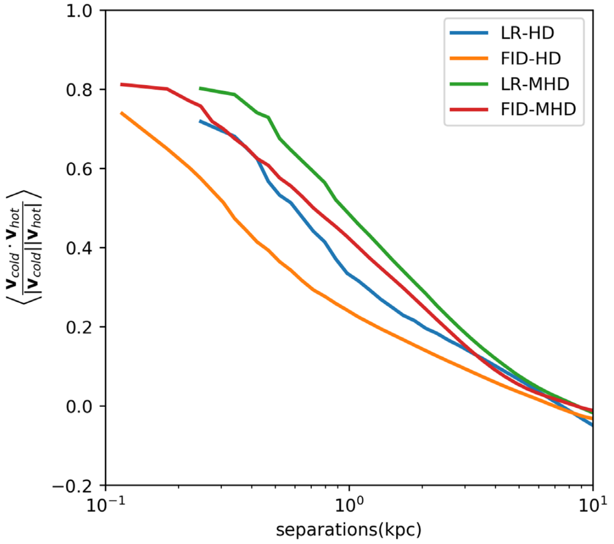

Figure 8. Average spatial correlation of the cold and hot velocity normalized by the velocity magnitude.

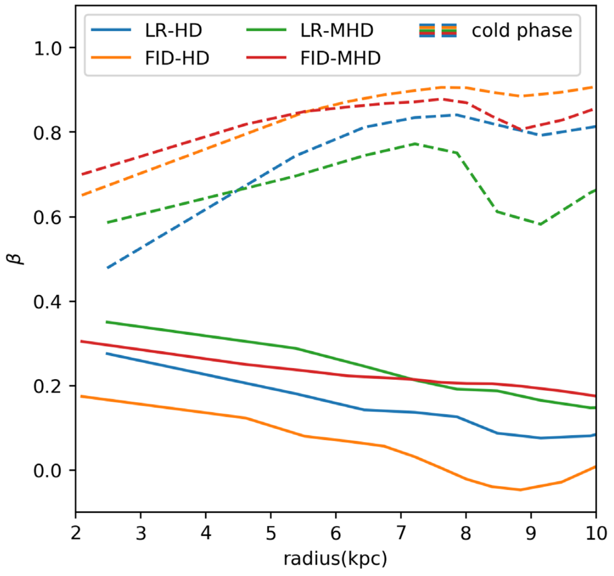

Figure 9. Average radial profile of the anisotropy parameter (β) of the hot gas in all runs. β of the cold gas is shown as dashed lines. Positive values of β correspond to radial bias in the velocity distribution.

process of decay of hot phase turbulence, the tangential motions should be progressively more important than the radial motions (e.g. Ruszkowski & Oh 2010) due to buoyant restoring forces. So the fact the hot gas motions are nevertheless radially biased suggests that they may be driven by the cold gas.

We note that the radial bias in the velocity distribution of the hot phase is unlikely to be caused by anisotropy in the radial hot gas accretion or the ‘gentle circulation’ described in Yang & Reynolds (2016b). As explained below, the inflow velocities due to these two mechanisms are both much smaller than the values of the hot gas VSF (except at very small separations).

The average AGN cold mass accretion rates over the first Gyr of all runs are in the range 40–70 $\mathrm{M_\odot}$ $\mathrm{yr^{-1}}$. The estimated hot mode accretion rate is $\dot{M} \lesssim 1\,\mathrm{M_\odot}$ $\mathrm{yr^{-1}}$ as it is expected to be ∼2 orders of magnitude smaller than that of the cold mode (Gaspari et al. 2013). This accretion rate corresponds to an inflow velocity $v_{\mathrm{in,hot}} \sim \dot{M}/4\pi r^2\rho_{\mathrm{ICM}}$. For $r = 10\,\mathrm{kpc}$ and $\rho_{\mathrm{ICM}} \approx 10^{-25}\,\mathrm{g\,cm^{-3}}$, the inflow velocity is only $v_{\mathrm{in,\,hot}} \lesssim 0.6\,\mathrm{km\,s^{-1}}$.

The ambient gas outside of the jet cone can form a reduced cooling flow (Yang & Reynolds 2016b). Assuming this inflow replenishes the gas mass in the central region lost to the bipolar outflow, the inflow velocity ($v_{\mathrm{in,\,circ}}$) can be estimated from:

$$v_{\mathrm{in,circ}} = \frac{2\Omega}{4\pi - 2\Omega}\frac{\rho_{\mathrm{jet}}}{\rho_{\mathrm{ICM}}}v_{\mathrm{jet}}, \tag{9}$$

where Ω is the solid angle subtended by the jet cone; ρ_{jet} and ρ_{ICM} are the gas density of jet and ambient ICM respectively; and v_{jet} is the jet velocity. Estimating right-hand side quantities at $r \approx 10\,\mathrm{kpc}$ to be $\Omega \approx 0.2$ (for jet cone apex angle equals to 30 deg), $\rho_{\mathrm{jet}}/\rho_{\mathrm{ICM}} \approx 0.1$, and $v_{\mathrm{jet}} \lesssim 5000\,\mathrm{km\,s^{-1}}$, the estimated inflow velocity is only $v_{\mathrm{in,\,circ}} \lesssim 17\,\mathrm{km\,s^{-1}}$.

3.3.2 Turbulence driving by AGN

AGN jets can be an important source of turbulence in the hot phase. In order to disentangle the contributions of AGN and cold filaments to hot phase VSF, we perform four test simulations with the same initial conditions as the four full physics simulations, but excluding radiative cooling and enforcing constant AGN jet power. The constant AGN power is chosen to be consistent with the average AGN power in the production runs within the first 1 Gyr. We note that all four full physics simulations inject almost identical amount of energy during this time interval, which simplifies the interpretation of the results.

These test simulations demonstrate that the AGN jets effectively transfer momentum to the hot ambient gas (i.e. the hot gas outside of the jet cone) when the magnetic fields are present. Specifically, Fig. 10 shows the slice plots of $|v_x|$ for the test simulations. It is clear from this figure that the ambient gas moves much faster in the MHD case compared to the hydro case. This implies that the magnetic fields in the centre of the cluster facilitate the momentum transfer from the jets to the ambient region.

Fig. 11 shows the averaged VSF of hot phase gas in the production runs and those in the corresponding test runs. In this figure, we consider LR-HD and LR-MHD cases as we evolved them for the longest time. However, we also note that FID-HD and FID-MHD evolved up to ∼0.6 Gyr were convergent when compared to their lower resolution counterparts both in terms of the normalization and slope of the VSF. In the hydro cases, the motion induced by the AGN only is subdominant (orange dotted lines in the left-hand panel), so it is likely that the hot phase motion is mainly driven by cold filaments in this case. In the MHD cases, the VSF contribution from the AGN only (orange dotted line in the right-hand panel) is comparable to that due to the combination of the filaments and AGN in the full physics case, indicating that the motion driver of the hot gas could be a mixture of the AGN jet and cold filament stirring. This is likely due to better coupling of the jets with the ambient medium facilitated by the presence of the magnetic fields. Additionally, this picture is further supported by comparing the normalization of the hot and cold VSF (left four panels of Fig. 4). In the hydro cases, the cold phase VSF has higher velocity normalization than the hot phase VSF on all scales, so the massive cold filaments with high velocity may be sufficiently energetic to drive turbulence in the hot phase. In the MHD cases, at large scale, the hot VSF has higher normalization than the cold VSF, indicating the turbulence in hot phase must be driven by other means.

We note that our manual jet case scenario is similar to the one considered by Hillel & Soker (2020). In their simulations, the hot

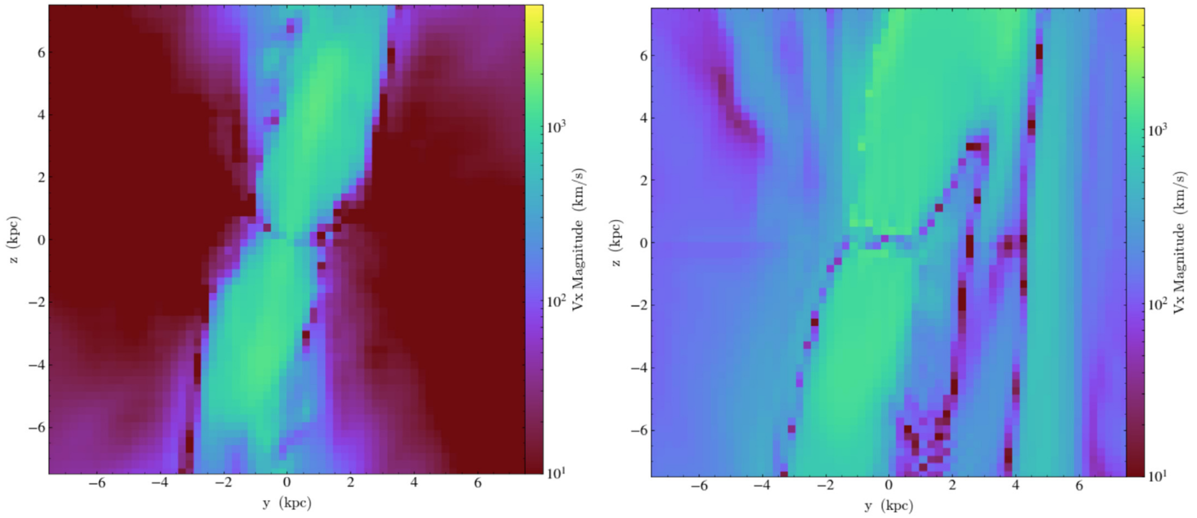

Figure 10. Snapshots of the slice plot of $|v_x|$ in the test simulations with AGN manually turned-on. Left-hand panel is for the test run with the same initial conditions as in the LR-HD run and the right-hand panel corresponds to the same initial conditions as in the LR-MHD run.

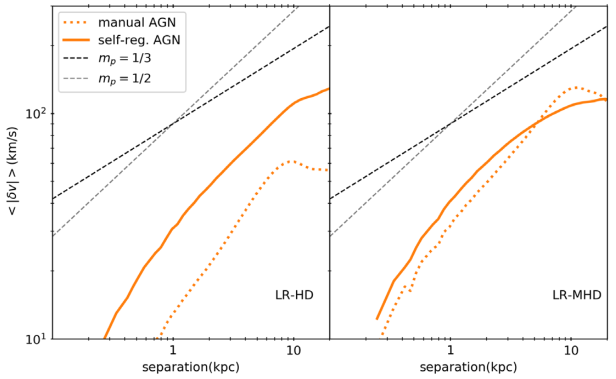

Figure 11. Averaged VSF of the hot gas in self-regulated AGN simulations (solid lines) and in the corresponding test simulations with manually turned-on AGN (dot line). The VSFs are averaged over $t = 0$–1 Gyr.

phase VSF slope is 1/2, i.e. steeper than Kolmogorov, which is what we also find in our case in general. Since their simulations are too short for the local thermal instability to trigger the formation of precipitating clouds, and they neglect magnetic fields, the efficient stirring of the ICM in their case was likely facilitated by considering wide jet opening angle (half opening angle = 70 deg) to better couple the jet to the ambient medium. In our case, direct stirring of the ICM by the jet is less efficient because the jet is narrow and the precession angle is only 15 deg. Alternatively, jet intermittency considered by Hillel & Soker (2020) could also contribute to the differences in the efficiency of the coupling of the jet energy to the ICM (perhaps even while enforcing the same average jet luminosity), though we note that more bursty AGN activity is more efficient in generating sound waves than gentler AGN activity (Bambic & Reynolds 2019).

4 SUMMARY

We perform 3D MHD simulations to study the properties of turbulence in the multiphase ICM affected by self-regulated AGN feedback. We find that, in general, the first-order velocity structure function of the multiphase ICM is steeper than the slope predicted from Kolmogorov's theory ($m_p > 1/3$). Specifically we show that,

(i) the turbulent motions of the cold gas are primarily driven by the gravitational acceleration. This leads to the cold phase VSF slope close to 1/2. When magnetic fields are included, the magnetic tension decelerates the cold gas and the VSF slope is either close to 1/2 or slightly shallower.

(ii) Without the influence of magnetic fields, the precipitating cold filaments are likely the dominant driving source of the turbulence in the ambient hot ICM. The arguments in favour of this hypothesis are: (i) in the central region of the gaseous halo, cold filaments have sufficient momentum to drive motions in the ambient hot gas; (ii) velocities of hot and cold phases are spatially correlated; (iii) in the absence of magnetic fields, the slope of hot gas VSF during AGN active phase is steeper than 1/3 and matches that of the cold phase; (iv) both hot and cold phase velocities are radially biased.

(iii) When magnetic fields are included, turbulence in the hot phase may be driven by a combination of AGN jet stirring and filament motion. This is because the magnetic fields facilitate the AGN driving by enhanced coupling between jet-like outflow and the ambient hot gas.

(iv) We find tentative evidence for the flattening of the hot phase VSF in the MHD case (see Fig. 6). However, in this case, we cannot draw definite conclusions on the slope of the hot phase VSF due to narrower inertial range and lack of numerical convergence.

ACKNOWLEDGEMENTS

We thank the anonymous referee for a very useful report. We thank Daisuke Nagai and Prateek Sharma for helpful suggestions. We thank Yuan Li for interesting discussions. Resources supporting this work were provided by the NASA High-End Computing (HEC) Program through the NASA Advanced Supercomputing (NAS) Division at Ames Research Center. MR acknowledges support from NSF Collaborative Research Grants AST-1715140 and AST-2009227, and NASA grants 80NSSC20K1541 and 80NSSC20K1583. CP acknowledges support by the European Research Council under ERC-CoG grant CRAGSMAN-646955. HYKY acknowledges support from NASA ATP (NNX17AK70G), Yushan Scholar Program of the Ministry of Education of Taiwan, and ⟨0:funding-source 3: href="http://dx.doi.org/10.13039/501100004663"⟩Ministry of Scie nce and Technology of Taiwan⟨/0:funding-source⟩ (MOST 109-

2112-M-007-037-MY3). SPO acknowledges support from NASA grants NNX17AK58G, 80NSSC20K0539, and NSF grant AST-1911198. This research was initiated at the 'Multiscale phenomena in plasma astrophysics' workshop at the Kavli Institute for Theoretical Physics in Santa Barbara. This research was supported in part by the National Science Foundation under grant no. NSF PHY-1748958.

DATA AVAILABILITY

The data underlying this article will be shared on reasonable request to the corresponding author.

REFERENCES

Abdulla Z. et al., 2019, ApJ, 871, 195

Babyk I. V., McNamara B. R., Tamhane P. D., Nulsen P. E. J., Russell H. R., Edge A. C., 2019, ApJ, 887, 149

Bambic C. J., Reynolds C. S., 2019, ApJ, 886, 78

Beckmann R. S. et al., 2019, A&A, 631, A60

Bîrzan L. et al., 2020, MNRAS, 496, 2613

Bourne M. A., Sijacki D., 2017, MNRAS, 472, 4707

Bourne M. A., Sijacki D., Puchwein E., 2019, MNRAS, 490, 343

Churazov E., Forman W., Jones C., Böhringer H., 2003, ApJ, 590, 225

Churazov E., Ruszkowski M., Schekochihin A., 2013, MNRAS, 436, 526

Dubey A., Reid L., Fisher R., 2008, Phys. Scr., 2008, 014046

Ehlert K., Weinberger R., Pfrommer C., Pakmor R., Springel V., 2018, MNRAS, 481, 2878

Ehlert K., Pfrommer C., Weinberger R., Pakmor R., Springel V., 2019, ApJ, 872, L8

Ehlert K., Weinberger R., Pfrommer C., Springel V., 2021, MNRAS, preprint(arXiv:2011.13964)

Fabian A. C., Johnstone R. M., Sanders J. S., Conselice C. J., Crawford C. S., Gallagher J. S. I., Zweibel E., 2008, Nature, 454, 968

Frisbie R. L. S. et al., 2020, ApJ, 899, 159

Fryxell B. et al., 2000, ApJS, 131, 273

Gaspari M., Ruszkowski M., Sharma P., 2012, ApJ, 746, 94

Gaspari M., Ruszkowski M., Oh S. P., 2013, MNRAS, 432, 3401

Guo F., Oh S. P., 2008, MNRAS, 384, 251

Hillel S., Soker N., 2020, ApJ, 896, 104

Hitomi Collaboration, 2016, Nature, 535, 117

Hitomi Collaboration, 2018, PASJ, 70, 9

Iapichino L., Niemeyer J. C., 2008, MNRAS, 388, 1089

Jacob S., Pfrommer C., 2017a, MNRAS, 467, 1449

Jacob S., Pfrommer C., 2017b, MNRAS, 467, 1478

Lakhchaura K. et al., 2018, MNRAS, 481, 4472

Lau E. T., Gaspari M., Nagai D., Coppi P., 2017, ApJ, 849, 54

Lee D., 2013, J. Comput. Phys., 243, 269

Lee D., Deane A. E., 2009, J. Comput. Phys., 228, 952

Li Y. et al., 2020, ApJ, 889, L1

Li Y., Ruszkowski M., Bryan G. L., 2017, ApJ, 847, 106

Martizzi D., Quataert E., Faucher-Giguère C.-A., Fielding D., 2019, MNRAS, 483, 2465

Mathews W. G., Faltenbacher A., Brighenti F., 2006, ApJ, 638, 659

McCourt M., Sharma P., Quataert E., Parrish I. J., 2012, MNRAS, 419, 3319

McNamara B. R., Russell H. R., Nulsen P. E. J., Hogan M. T., Fabian A. C., Pulido F., Edge A. C., 2016, ApJ, 830, 79

Navarro J. F., Frenk C. S., White S. D. M., 1996, ApJ, 462, 563

Ogorzalek A. et al., 2017, MNRAS, 472, 1659

Olivares V. et al., 2019, A&A, 631, A22

Prasad D., Sharma P., Babul A., 2015, ApJ, 811, 108

Prasad D., Sharma P., Babul A., 2018, ApJ, 863, 62

Pulido F. A. et al., 2018, ApJ, 853, 177

Qiu Y., Bogdanović T., Li Y., McDonald M., 2019, ApJ, 872, L11

Ruszkowski M., Oh S. P., 2010, ApJ, 713, 1332

Ruszkowski M., Brüggen M., Begelman M. C., 2004a, ApJ, 611, 158

Ruszkowski M., Brüggen M., Begelman M. C., 2004b, ApJ, 615, 675

Ruszkowski M., Enßlin T. A., Brüggen M., Heinz S., Pfrommer C., 2007, MNRAS, 378, 662

Ruszkowski M., Lee D., Brüggen M., Parrish I., Oh S. P., 2011, ApJ, 740, 81

Ruszkowski M., Yang H. Y. K., Reynolds C. S., 2017, ApJ, 844, 13

Ruszkowski M., Yang H. Y. K., Reynolds C. S., 2018, ApJ, 858, 64

Sanders J. S., Fabian A. C., 2013, MNRAS, 429, 2727

Sharma P., Parrish I. J., Quataert E., 2010, ApJ, 720, 652

Sharma P., McCourt M., Quataert E., Parrish I. J., 2012, MNRAS, 420, 3174

Simionescu A. et al., 2019, Space Sci. Rev., 215, 24

Sutherland R. S., Dopita M. A., 1993, ApJS, 88, 253

Vantyghem A. N. et al., 2018, ApJ, 863, 193

Voit G. M., Donahue M., O'Shea B. W., Bryan G. L., Sun M., Werner N., 2015, ApJ, 803, L21

Voit G. M., Meece G., Li Y., O'Shea B. W., Bryan G. L., Donahue M., 2017, ApJ, 845, 80

Wang C., Li Y., Ruszkowski M., 2019, MNRAS, 482, 3576

Wang C., Ruszkowski M., Yang H. Y. K., 2020, MNRAS, 493, 4065

Weinberger R., Ehlert K., Pfrommer C., Pakmor R., Springel V., 2017, MNRAS, 470, 4530

Werner N. et al., 2013, ApJ, 767, 153

Werner N. et al., 2014, MNRAS, 439, 2291

Yang H. Y. K., Reynolds C. S., 2016a, ApJ, 829, 90

Yang H. Y. K., Reynolds C. S., 2016b, ApJ, 829, 90

Yang H. Y. K., Gaspari M., Marlow C., 2019, ApJ, 871, 6

Yoo H., Cho J., 2014, ApJ, 780, 99

Zhuravleva I. et al., 2014, Nature, 515, 85

Zhuravleva I., Churazov E., Kravtsov A., Sunyaev R., 2012, MNRAS, 422, 2712

Zinger E., Dekel A., Birnboim Y., Kravtsov A., Nagai D., 2016, MNRAS, 461, 412

ZuHone J. A., Markevitch M., Zhuravleva I., 2016, ApJ, 817, 110

ZuHone J. A., Miller E. D., Bulbul E., Zhuravleva I., 2018, ApJ, 853, 180

APPENDIX A: DRIVEN TURBULENCE TEST AND INERTIAL RANGE

In order to verify that the expected reference value of the hot phase VSF slope is indeed 1/3, and to assess at what minimum separations numerical effects become important, we perform controlled turbulence experiment neglecting AGN feedback, magnetic fields, radiative cooling, and gravity. In this idealized test, turbulence is driven via a spectral forcing scheme utilizing an Ornstein–Uhlenbeck random process. The spectral forcing scheme is set to stir the hot halo via a time-correlated, stochastic forcing with a narrow spectral range corresponding to ∼10 kpc. We use the same implementation of this scheme and model parameters as described in Ruszkowski & Oh (2010). The computational volume in this test is uniformly refined and the resolution is the same as in the FID-HD and FID-MHD cases.

After ∼250 Myr, the turbulent dissipation balances the energy injection rate due to the forcing and the 3D rms velocity stabilizes at $\sim 150\,\mathrm{km\,s^{-1}}$ (top panel in Fig. A1). Variations are caused in part by the fact that we use finite correlation time-scale for the driving forces (∼100 Myr). This is reflected in the top panel in Fig. A1 that shows that characteristic time-scale for the fluctuations in the velocity dispersion is about 100 Myr.

As expected, the VSF reaches a stable state, where the VSF follows the Kolmogorov prediction in the inertial range with the averaged slope equal to $m_{\mathrm{kol}} = 1/3$. The fluctuations in the slope are again a direct consequence of the finite correlation time-scale and fluctuations in the overall level of velocity dispersion. The VSF slope steepens on sub-kpc scales (bottom panel in Fig. A1). This indicates that the steepening of the VSF on sub-kpc scales is numerical in origin.

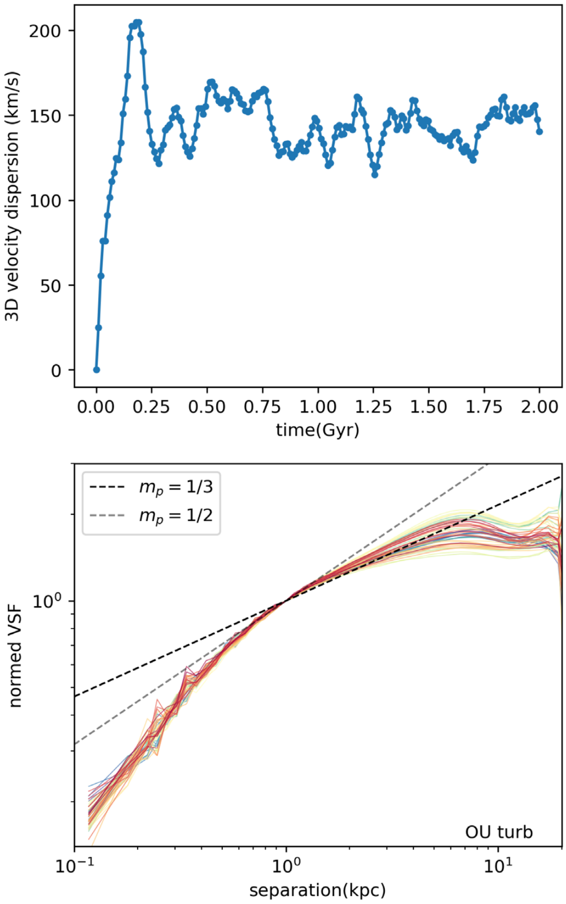

Figure A1. Top panel: time evolution of the 3D velocity dispersion in the driving turbulence test (see Appendix A). Bottom panel: VSFs plotted every 10 Myr from $t = 1$ to 1.5 Gyr for the driving turbulence test. The colour scheme is the same as Fig. 6.

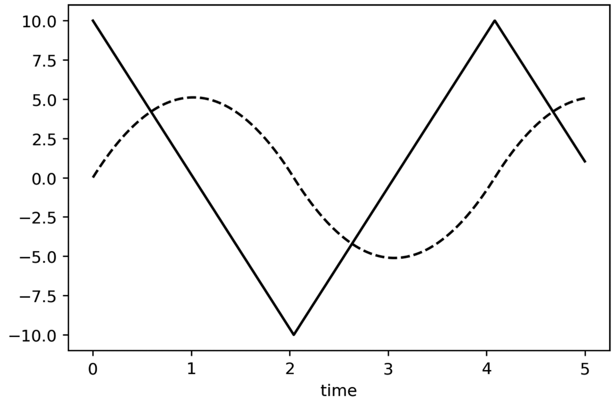

Figure B1. Time evolution of velocity (solid) and position (dashed line) of a test particle in a 1D gravitational potential $g_{\rm test}(x)$ (see Appendix B). All quantities are in arbitrary units.

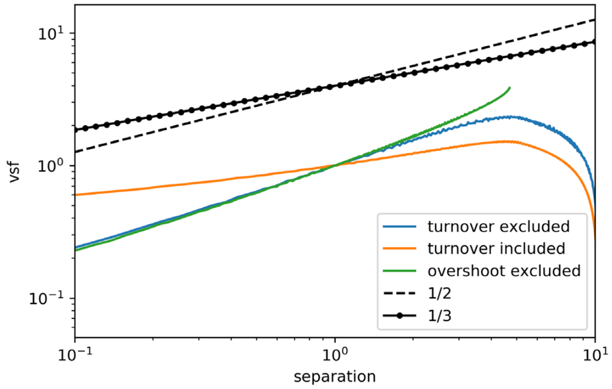

Figure B2. VSF of velocities and positions sampled from the trajectory of motion dominated by gravity. The meaning of colour is the same as Fig. B1.

APPENDIX B: VSF OF IDEALIZED MOTION DOMINATED BY GRAVITY

In order to investigate the VSF slope resulting from motions dominated by gravity, we perform a simple 1D calculation. We consider the motion of a test particle falling in the gravitational field $g_{\rm test}(x) = -{\rm sign}(x) g_0$, where g_0 is a constant (note that the gravitational acceleration in the central region of the cluster is approximately constant, which simplifies our analysis of the impact of gravity on the motions of cold gas clouds; see Fig. 5). The time evolution of the particle velocity and position are shown in Fig. B1. We sample the velocities and positions on this trajectory and calculate the VSF. In Fig. B2, we show VSFs corresponding to three different sampling cases: (i) when we sample the part of the trajectory that does not include overshooting through the very centre (time range from 1 to 2 in Fig. B1), the VSF slope is close to or slightly above 1/2 (green line in Fig. B2); (ii) when we exclude the the times past the turnover where velocity changes sign (i.e. when we consider the time range from 1 to 3), the VSF slope is close to 1/2 (blue line in Fig. B2); (iii) when sampling over a longer trajectory that includes the turnover (time ranging from 0 to 5), the VSF slope is close to 1/3 (orange line in Fig. B2).

Our full physics simulation results imply that rather than getting launched by the jet from the centre and raining back, most of the cold filaments form in the atmosphere and fall towards the centre. In Fig. B3, we show the amount of cold gas that is inflowing (blue lines) and outflowing (orange lines). It is evident from this figure that the inflow dominates over outflow in our simulations, consistent with previous works (e.g. Prasad et al. 2015). The infalling cold clouds either get accreted by the black hole or collide with the preexisting cold gas clumps. Therefore, the velocity magnitude of the clouds is damped by the collisions with the pre-existing cold gas as they overshoot the centre of the cluster. This situation corresponds approximately to the case in between (i) and (ii) above, where the expected slope is either 1/2 or slightly above it. As our simple experiment also demonstrates that longer sampling time range results in flatter VSF slopes. As the actual magnitude of the cloud velocity is expected to be damped over time, this simple test shows that the velocities and positions sampled from a free-falling trajectory can lead to the VSF slope close to ∼1/2 as seen in the full physics simulations.

As mentioned in the main text, the effect of the magnetic fields is to decelerate the clouds, which may further flatten the slope below 1/2. Interestingly, the dynamical effect of the magnetic fields are also seen in Fig. B3. Top and bottom panels in this figure corresponds to the FID-HD and FID-MHD cases, respectively. This figure shows that in the FID-MHD case outflow is even more subdominant compared to inflow. This is consistent with stronger damping of motions by the magnetic tension, especially as the clouds get closer to the centre, which reduces the tendency of the infalling cold gas to overshoot the centre.

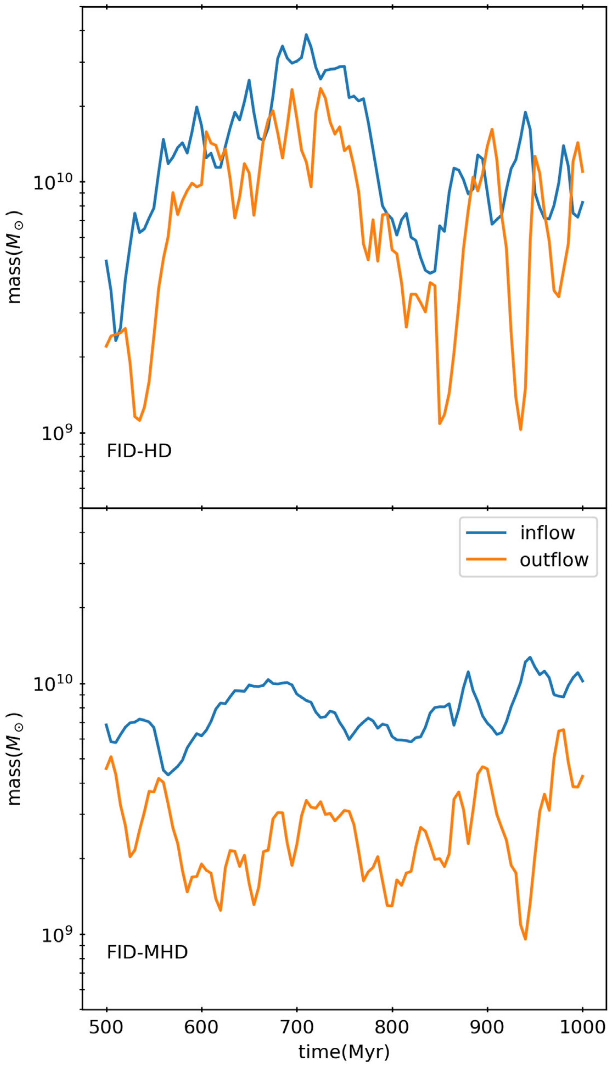

Figure B3. The evolution of the inflowing (blue lines) and ouftlowing (oragne lines) cold gas mass. Top panel corresponds to the FID-HD case and the bottom one to the FID-MHD case.

Since the objective of this simple experiment is to provide a proof of concept for the idea that ballistic (or nearly ballistic) motions can account for the cold phase VSF slopes, we choose not to pursue a more detailed analysis including additional free parameters such as the cloud velocity damping time or the distributions of heights from which the clouds are released, etc.

This paper has been typeset from a TEX/LATEX file prepared by the author.